






Efficient conversion of orbital Hall current to spin current for spin-orbit torque switching

Soogil Lee^{1,6} , Min-Gu Kang^{1,6}, Dongwook Go^{2,3}, Dohyoung Kim¹, Jun-Ho Kang⁴, Taekhyeon Lee⁴, Geun-Hee Lee⁴, Jaimin Kang¹, Nyun Jong Lee⁵, Yuriy Mokrousov^{2,3} , Sanghoon Kim⁵ , Kab-Jin Kim⁴, Kyung-Jin Lee⁴  & Byong-Guk Park¹  [✉]

Spin Hall effect, an electric generation of spin current, allows for efficient control of magnetization. Recent theory revealed that orbital Hall effect creates orbital current, which can be much larger than spin-Hall-induced spin current. However, orbital current cannot directly exert a torque on a ferromagnet, requiring a conversion process from orbital current to spin current. Here, we report two effective methods of the conversion through spin-orbit coupling engineering, which allows us to unambiguously demonstrate orbital-current-induced spin torque, or orbital Hall torque. We find that orbital Hall torque is greatly enhanced by introducing either a rare-earth ferromagnet Gd or a Pt interfacial layer with strong spin-orbit coupling in Cr/ferromagnet structures, indicating that the orbital current generated in Cr is efficiently converted into spin current in the Gd or Pt layer. Our results offer a pathway to utilize the orbital current to further enhance the magnetization switching efficiency in spin-orbit-torque-based spintronic devices.

¹Department of Materials Science and Engineering and KI for Nanocentury, KAIST, Daejeon 34141, Korea. ²Peter Grünberg Institut and Institute for Advanced Simulation, Forschungszentrum Jülich and JARA, Jülich 52425, Germany. ³Institute of Physics, Johannes Gutenberg University Mainz, Mainz 55099, Germany. ⁴Department of Physics, KAIST, Daejeon 34141, Korea. ⁵Department of Physics, University of Ulsan, Ulsan 44610, Korea. ⁶These authors contributed equally: Soogil Lee, Min-Gu Kang. ✉email: bgpark@kaist.ac.kr

Spin Hall effect (SHE) that creates a transverse spin current by a charge current in a non-magnet (NM) with strong spin-orbit coupling (SOC)¹ has received much attention because the resulting spin-orbit torque (SOT) offers efficient control of magnetization in NM/ferromagnet (FM) heterostructures of various spintronic devices^{2–9}. Similar to the SHE, the orbital Hall effect (OHE) generates an orbital current, a flow of orbital angular momentum^{10–13}. The OHE has distinctive features compared to the SHE; first, the OHE originates from momentum-space orbital textures, so it universally occurs in multi-orbital systems regardless of the magnitude of SOC¹². For example, it has been reported non-trivial orbital current can be generated in 3d transition metals, graphene, or two-dimensional transition metal dichalcogenides^{13–18}. Second, theoretical calculations show that orbital Hall conductivity is much larger than spin Hall conductivity in many materials, including those commonly used for SOT such as Ta and W^{10,11,13}. This suggests that the spin torque caused by the OHE, or orbital Hall torque (OHT)^{19,20}, can be larger than the SHE-induced spin torque, enhancing the spin-torque efficiency in spintronic devices. Recently, several experimental reports have claimed that significant SOT and magnetoresistance observed in FM/Cu/oxide structures, in which the SHE is known to be negligible, is of orbital current origin^{21–24}. However, it seems that the underlying mechanism of the OHE and associated OHT are not yet fully understood. One issue is that there is no exchange coupling between orbital angular momentum (L) and local magnetic moment, and thus the orbital current cannot directly give a torque on magnetization. To make the OHT exerts on the local magnetic moment of the FM, the L must be converted to the spin angular momentum (S)^{19,20}. Therefore, finding an efficient method of “ L - S conversion” is crucial to utilizing the OHT for the manipulation of the magnetization direction.

In this article, we experimentally demonstrate two effective L - S conversion techniques of engineering SOC of either an FM or an NM/FM interface. We employ Cr as an orbital current source material because it has been theoretically predicted that Cr has a large orbital Hall conductivity $\sigma_{\text{OH}}^{\text{Cr}}$ of ~ 8200 (\hbar/e)(Ω cm)⁻¹ while having a relatively small spin Hall conductivity $\sigma_{\text{SH}}^{\text{Cr}}$ of -130 (\hbar/e)(Ω cm)⁻¹ with the opposite sign¹³. Here, \hbar is the reduced Planck constant and e is the electron charge. For the Cr/FM bilayers, overall charge-to-spin conversion efficiency referred as effective spin Hall angle $\theta_{\text{SH}}^{\text{eff}}$, is expressed as¹⁹

$$\theta_{\text{SH}}^{\text{eff}} = (2e/\hbar)(\sigma_{\text{SH}}^{\text{Cr}} + \sigma_{\text{OH}}^{\text{Cr}}\eta_{L-S})/\sigma_{xx}^{\text{Cr}}, \quad (1)$$

where σ_{xx}^{Cr} is the electrical conductivity of Cr and η_{L-S} is the L - S conversion coefficient. Here, we assume perfect transmission ($T_{\text{int}} = 1$) of both spin and orbital currents through the Cr/FM interface. Note that the second term on the right side of Eq. (1) corresponds to the OHE contribution to $\theta_{\text{SH}}^{\text{eff}}$, which depends on the magnitude and sign of η_{L-S} . We demonstrate how to achieve a large η_{L-S} by engineering the SOC of an FM or an NM interfacial layer. First, we employ a rare-earth FM of Gd with strong SOC, which increases the OHT in Cr/Gd heterostructures by ten times compared to that in Cr/Co heterostructures, indicating that the orbital current generated in Cr is efficiently converted to spin current in the FM Gd layer. Second, we modify the Cr/Co₃₂Fe₄₈B₂₀ (CoFeB) interface by inserting a 1 nm Pt layer to facilitate L - S conversion. This leads to an enhancement in OHT, allowing us to demonstrate OHT-induced magnetization switching of perpendicular magnetization in Cr/Pt/CoFeB heterostructures. Since the OHE is expected to occur generally in various materials, our results demonstrating the significant OHT generated through the L - S conversion techniques broaden the scope of material engineering to improve spin-torque switching efficiency for the development of low-power spintronic devices.

Results and discussion

Orbital Hall torque generated by orbital current in Cr. To demonstrate the OHE in Cr and associated OHT, we investigate the current-induced spin-torque in Cr/FM heterostructures for two different FMs of Co and Ni. Figure 1a, b illustrates the role of η_{L-S} in $\theta_{\text{SH}}^{\text{eff}}$ of the Cr/FM samples, where S_{SHE} is the spin angular momentum generated by SHE and S_{OHE} is the spin angular momentum converted from orbital angular momentum due to OHE (L_{OHE}). Note that we assume that Ni has a greater η_{L-S} than that of Co ($\eta_{L-S}^{\text{Ni}} > \eta_{L-S}^{\text{Co}}$) because $\sigma_{\text{SH}}^{\text{Ni}}$ is an order of magnitude larger than $\sigma_{\text{SH}}^{\text{Co}}$ ^{25,26}. This is also supported by a recent first principle calculation demonstrating that the W/Ni bilayer exhibits a positive $\theta_{\text{SH}}^{\text{eff}}$ despite the negative $\sigma_{\text{SH}}^{\text{W}}$ of W²⁰. This is attributed to the increased orbital current contribution to $\theta_{\text{SH}}^{\text{eff}}$ by the large and positive η_{L-S}^{Ni} . Figure 1a shows the case of a Cr/Co bilayer with $\eta_{L-S}^{\text{Co}} \sim 0$, where S_{SHE} is dominant and thus $\theta_{\text{SH}}^{\text{eff}}$ is mainly determined by $\sigma_{\text{SH}}^{\text{Cr}}$ of negative sign. On the other hand, for the Cr/Ni bilayer having sizable η_{L-S}^{Ni} , non-negligible S_{OHE} caused by the conversion of $\sigma_{\text{OH}}^{\text{Cr}}$ contributes to $\theta_{\text{SH}}^{\text{eff}}$ (Fig. 1b). Since S_{OHE} is a positive value ($\eta_{L-S}^{\text{Ni}} > 0$ & $\sigma_{\text{OH}}^{\text{Cr}} > 0$), opposite to S_{SHE} , $\theta_{\text{SH}}^{\text{eff}}$ of the Cr/Ni heterostructures becomes positive when the magnitude of S_{OHE} is larger than that of S_{SHE} . To test whether the orbital current generated in Cr gives rise to OHT, we perform in-plane harmonic Hall measurements of Co (3.0 nm)/Cr (7.5 nm) and Ni (2.0 nm)/Cr (7.5 nm) Hall-bar patterned samples (Fig. 1c). Figure 1d, e shows representative second harmonic Hall resistance ($R_{xy}^{2\omega}$) versus azimuthal angle (φ) curves under different external magnetic fields (B_{ext}). $R_{xy}^{2\omega}(\varphi)$ is expressed as²⁷

$$R_{xy}^{2\omega}(\varphi) = \{[R_{\text{AHE}}^{1\omega}(B_{\text{DLT}}/B_{\text{eff}}) + R_{\text{VT}}]\cos\varphi + [2R_{\text{PHE}}^{1\omega}(B_{\text{FLT}} + B_{\text{Oe}})/B_{\text{ext}}](2\cos^3\varphi - \cos\varphi)\}, \quad (2)$$

where $R_{\text{AHE}}^{1\omega}$ and $R_{\text{PHE}}^{1\omega}$ are the first harmonic anomalous Hall and planar Hall resistances, respectively; B_{DLT} (B_{FLT}) is the damping-like (field-like) effective field; B_{eff} is the effective magnetic field, including the demagnetization field and anisotropy field of FM; R_{VT} is the thermal contributions, and B_{Oe} is the current-induced Oersted field. The $R_{\text{AHE}}^{1\omega}$ and $R_{\text{PHE}}^{1\omega}$ data are shown in Supplementary Note 1. Figure 1f shows the $\cos\varphi$ component of $R_{xy}^{2\omega}$ divided by $R_{\text{AHE}}^{1\omega}$ [$R_{\text{cos}\varphi}^{2\omega}/R_{\text{AHE}}^{1\omega}$] as a function of $1/B_{\text{eff}}$ for the two FM/Cr samples, of which the slope represents B_{DLT} and associated $\theta_{\text{SH}}^{\text{eff}}$. We find that the Co/Cr sample shows a negative slope, and thus a negative $\theta_{\text{SH}}^{\text{eff}}$. This is consistent with the negative $\sigma_{\text{SH}}^{\text{Cr}}$ reported both theoretically and experimentally^{28–30}. In contrast, the Ni/Cr sample exhibits a positive slope, indicating a positive $\theta_{\text{SH}}^{\text{eff}}$. The sign reversal of $\theta_{\text{SH}}^{\text{eff}}$ in the Ni/Cr sample is attributed to the increased contribution of the orbital current in Cr by the L - S conversion in Ni ($\sigma_{\text{OH}}^{\text{Cr}}\eta_{L-S}^{\text{Ni}} > 0$). Note that the $(2\cos^3\varphi - \cos\varphi)$ component of $R_{xy}^{2\omega}$ divided by $R_{\text{PHE}}^{1\omega}$, representing $B_{\text{FLT}} + B_{\text{Oe}}$, of the Ni/Cr sample is larger than that of the Co/Cr sample. This might also be related to the increased orbital current in the Ni/Cr sample as discussed in Supplementary Note 2.

To verify whether the orbital current in Cr is the main cause of the measured torque, we perform two control experiments. First, we investigate the role of FM in determining $\theta_{\text{SH}}^{\text{eff}}$ by measuring the $R_{\text{cos}\varphi}^{2\omega}/R_{\text{AHE}}^{1\omega}$ of the Co (3 nm)/Pt (5 nm) and Ni (2 nm)/Pt (5 nm) structures, in which Cr is replaced by Pt, which has positive $\sigma_{\text{SH}}^{\text{Pt}}$ and $\sigma_{\text{OH}}^{\text{Pt}}$ ^{10,11,13,31}. Figure 1f shows positive slopes and corresponding positive $\theta_{\text{SH}}^{\text{eff}}$'s for both the FM/Pt samples, indicating that the sign change of $\theta_{\text{SH}}^{\text{eff}}$ in the FM/Cr samples is not due to the FM layer itself²⁶. Note that the damping-like torque

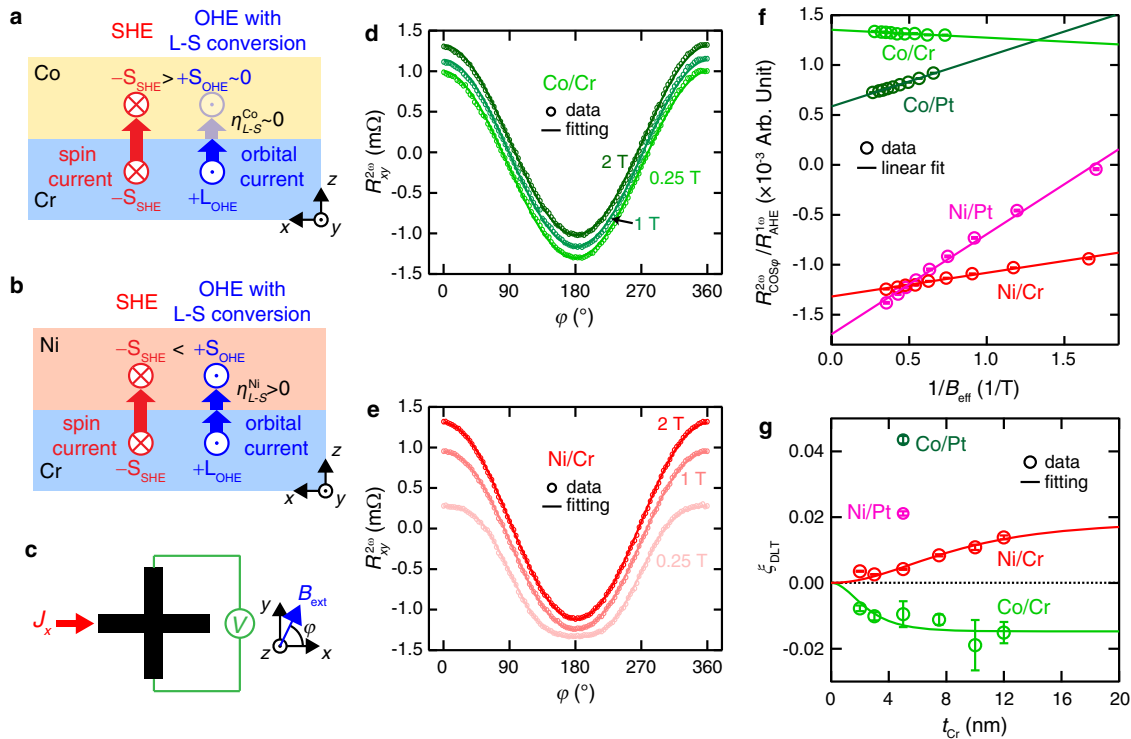


Fig. 1 Orbital-current-induced spin torque in Cr/ferromagnet heterostructures. **a, b** Schematic illustrations of the angular momentum transfer by spin current (red arrows) and orbital current (blue arrows) for Co (**a**) and Ni (**b**) ferromagnets (FMs). The spin (orbital) angular momentum is represented by S (L). The source of S and L is marked by the subscript of SHE (OHE) for spin Hall effect (orbital Hall effect). $\eta_{L-S}^{Co(Ni)}$ is the orbital-to-spin conversion efficiency of Co (Ni). **c** The $R_{xy}^{2\omega}(\varphi)$ measurement geometry for a Hall-bar sample. φ is the azimuthal angle of the external magnetic field (B_{ext}) with respect to the current direction. **d, e** Azimuthal angle (φ) dependent second harmonic Hall resistance, $R_{xy}^{2\omega}(\varphi)$, under different B_{ext} of Co (3.0 nm)/Cr (7.5 nm) (**d**) and Ni (2.0 nm)/Cr (7.5 nm) (**e**) samples. The solid lines are the fitting curves using Eq. (2). Each $R_{xy}^{2\omega}(\varphi)$ curve of Co/Cr (**d**) and Ni/Cr (**e**) is shifted by a y-axis offset to clearly show the B_{ext} dependence. **f** $R_{xy}^{2\omega}/R_{AHE}^{1\omega}$ as function of $1/B_{eff}$ of Ni/Cr (red), Co/Cr (light-green), Ni/Pt (magenta), and Co/Pt (green) samples. Each solid line is the linear fitting line. The error bars in **f** are due to the standard deviation of the fitting of the $R_{xy}^{2\omega}(\varphi)$ versus φ curves using Eq. (2), which are smaller than the symbol size. **g** Cr thickness (t_{Cr}) dependent damping-like torque efficiency (ξ_{DLT}) of Ni/Cr (red) and Co/Cr (light-green) samples, where t_{Cr} ranges from 2 to 12.5 nm. The fitting results of orbital and spin diffusion lengths for Ni/Cr and Co/Cr are given in solid curves. The ξ_{DLT} 's of the reference Ni/Pt (magenta) and Co/Pt (green) samples are included for comparison. Lines are guides to eyes. All measurements are conducted at 300 K. The error bars in **g** are due to the standard deviation of the linear fitting of the $\cos\varphi$ components of Eq. (2) versus $1/B_{eff}$.

efficiency³¹, $\xi_{DLT} = (2e/h)(M_S t_{FM} B_{DLT}/J_{Pt})$ where, M_S is the saturation magnetization, t_{FM} is the FM thickness, and J_{Pt} is the current density flowing in Pt (Supplementary Note 3), between the Co/Pt and Ni/Pt samples differs by a factor of two. This indicates that interface transmission (T_{int}) plays a critical role in determining ξ_{DLT} in these samples, where the spin current is primarily generated by the SHE in the Pt layer³². It implies that T_{int} can affect the ξ_{DLT} even in the FM/Cr sample, where the OHE is dominated. However, T_{int} cannot account for the different signs of the θ_{SH}^{eff} (or ξ_{DLT}) between the Co/Cr and Ni/Cr samples since it can only reduce the magnitude of the ξ_{DLT} by diminishing the transmission of spin (or orbital) currents. Second, we examine the interfacial contributions^{33–38} to θ_{SH}^{eff} by measuring the Cr thickness (t_{Cr}) dependence of the ξ_{DLT} for the FM/Cr samples. If the positive θ_{SH}^{eff} of the Ni/Cr samples is due to the interfacial effect, ξ_{DLT} decreases with increasing t_{Cr} and eventually changes its sign to negative for thicker t_{Cr} 's where bulk Cr with negative σ_{SH}^{Cr} dominates. However, this is not the case, as shown in Fig. 1g; for both FM/Cr samples, the magnitude of ξ_{DLT} increases with t_{Cr} , while maintaining its sign unchanged, which demonstrates that there is no significant interfacial contribution to θ_{SH}^{eff} in the FM/Cr samples. Note that we analyze the t_{Cr} dependence of ξ_{DLT} using a method of analyzing the SHE-induced SOT³¹, $\xi_{DLT} \sim [1 - \text{sech}(\frac{t_{Cr}}{\lambda_{Cr}})]$, where, λ_{Cr} is the spin or orbital diffusion

length. The extracted λ_{Cr} value is 6.1 ± 1.7 nm for the Ni/Cr and 1.8 ± 0.6 nm for the Co/Cr samples, which can be regarded as the orbital and spin diffusion lengths of Cr, respectively, since the ξ_{DLT} of the Ni/Cr (Co/Cr) sample is governed predominantly by the OHE (SHE). This result indicates that the orbital diffusion length is much greater than the spin diffusion length in Cr, as expected by theoretical calculations (Supplementary Note 4). These results corroborate that the OHE in Cr primarily governs the θ_{SH}^{eff} of the FM/Cr samples, providing an excellent platform to study L-S conversion engineering.

Efficient L-S conversion through rare-earth ferromagnet Gd.

We now present two techniques to enhance the η_{L-S} of the Cr/FM structures. First, we introduce a rare-earth FM Gd, which is expected to have a large η_{L-S} due to its strong SOC^{39,40}. Figure 2a illustrates the L-S conversion process in Cr/Gd heterostructures, where η_{L-S}^{Gd} is negative because of its negative spin Hall angle⁴¹. In this case, S_{OHE} due to the orbital current ($\eta_{L-S}^{Gd} \sigma_{OH}^{Cr} < 0$) is the same sign as S_{SHE} ($\sigma_{SH}^{Cr} < 0$), so they add up constructively with each other. This would result in enhanced θ_{SH}^{eff} in the Cr/Gd heterostructure compared to the Cr/Co heterostructure. To verify this idea, we prepare Hall-bar patterned samples of Gd (10 nm)/Cr (7.5 nm) and Co (10 nm)/Cr (7.5 nm) structures and conduct in-plane harmonic Hall measurements at 10 K to avoid any side

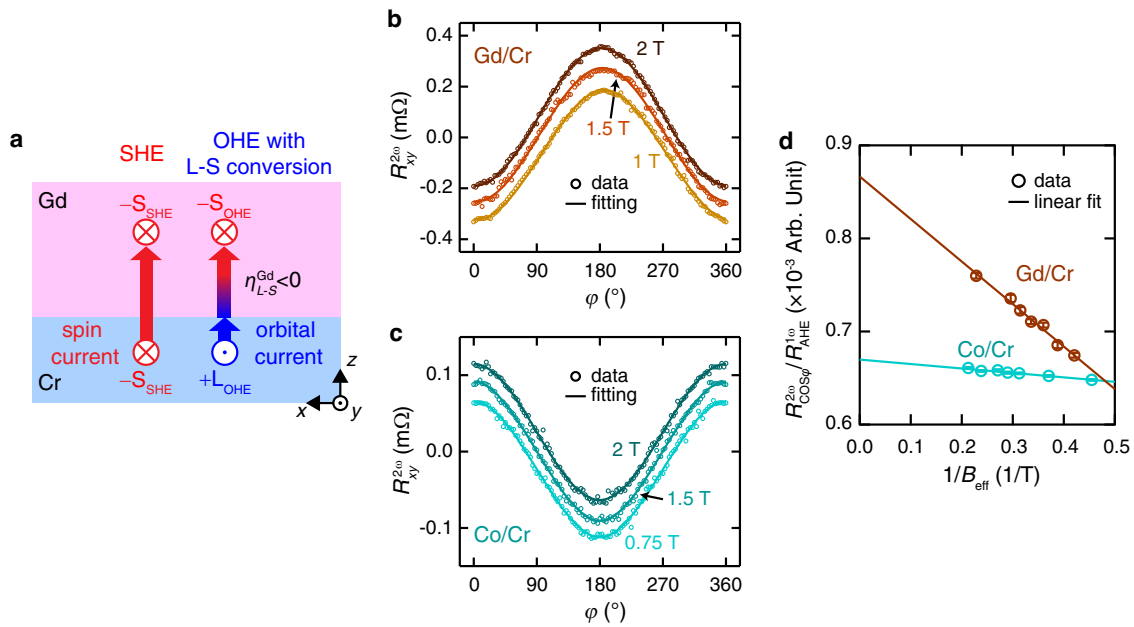


Fig. 2 Efficient orbital-to-spin conversion by rare-earth Gd with strong spin-orbit coupling. **a** Schematic illustration of the orbital-to-spin ($L-S$) conversion by η_{L-S}^{Gd} in the Cr/Gd heterostructure. The spin (orbital) angular momentum is represented by S (L). The source of S and L is marked by the subscript of SHE (OHE) for spin Hall effect (orbital Hall effect). **b**, **c** $R_{xy}^{2\omega}(\phi)$ under different B_{ext} of Gd (10 nm)/Cr (5 nm) (**b**) and Co (10 nm)/Cr (5 nm) (**c**) samples. Each $R_{xy}^{2\omega}(\phi)$ of Gd/Cr (**b**) and Co/Cr (**c**) is shifted by a y-axis offset to clearly show B_{ext} dependence. The solid lines are the fitting curves using Eq. (2). **d** $R_{xy}^{2\omega}/R_{AHE}^{1\omega}$ versus $1/B_{eff}$ of Gd/Cr (brown) and Co/Cr (blue-green) samples. Each solid line is the linear fitting line. All measurements are conducted at 10 K. The error bars in **d** are due to the standard deviation of the fitting of the $R_{xy}^{2\omega}(\phi)$ versus ϕ curves using Eq. (2), which are smaller than the symbol size.

effects due to the large difference in Curie temperatures between Gd (~ 293 K) and Co (~ 1400 K). Note that Cr is known to be antiferromagnetic at 10 K⁴², however, the exchange coupling of the Gd (Co)/Cr sample is negligibly small and therefore does not affect the harmonic Hall measurements (Supplementary Note 5). Figure 2b, c shows the $R_{xy}^{2\omega}(\phi)$ data measured under different B_{ext} 's of the Gd/Cr and Co/Cr samples, respectively, which are well described by Eq. (2) as represented by solid curves. The $R_{AHE}^{1\omega}$ and $R_{PHE}^{1\omega}$ data are shown in Supplementary Note 1. Figure 2d shows $R_{xy}^{2\omega}/R_{AHE}^{1\omega}$ versus $1/B_{eff}$ for the Gd/Cr and Co/Cr samples. We find two points; first, both samples exhibit negative slopes, indicating $\theta_{SH}^{eff} < 0$. Second, the Gd/Cr sample has a much larger slope or B_{DLT} than that of the Co/Cr sample. The estimated ξ_{DLT} of the Gd/Cr sample is -0.21 ± 0.01 , which is about ten times greater than that of the Co/Cr sample (-0.018 ± 0.002). Note that ξ_{DLT} of the Gd/Cr samples increases with the t_{Cr} (Supplementary Note 6), indicating that ξ_{DLT} originates from the orbital current in bulk Cr. The large enhancement of ξ_{DLT} or θ_{SH}^{eff} demonstrates that the OHT contribution can be increased by introducing FMs with large η_{L-S} .

We estimate effective spin Hall conductivity $\sigma_{SH}^{Cr}(eff) = \sigma_{SH}^{Cr} + \sigma_{OH}^{Cr}\eta_{L-S}$ of the samples using the relation³¹ $\sigma_{SH}^{Cr}(eff) = (\hbar/2e) \cdot (\xi_{DLT} \times \sigma_{xx}^{Cr})$. The calculated $\sigma_{SH}^{Cr}(eff)$ of the Gd/Cr sample is -999 (\hbar/e) $\cdot(\Omega\text{ cm})^{-1}$, which is much larger than the theoretical spin Hall conductivity of Cr¹³, $\sigma_{SH}^{Cr} = -130$ (\hbar/e) $\cdot(\Omega\text{ cm})^{-1}$. The large $\sigma_{SH}^{Cr}(eff)$ value of the Gd/Cr sample supports our claim that the enhanced ξ_{DLT} is due to the orbital current in Cr, subject to the effective conversion into spin currents in Gd ($\sigma_{OH}^{Cr}\eta_{L-S}^{Gd}$). On the other hand, the $\sigma_{SH}^{Cr}(eff)$ of the Co/Cr sample is -86 (\hbar/e) $\cdot(\Omega\text{ cm})^{-1}$, which is comparable to the theoretical σ_{SH}^{Cr} value. This is consistent with the fact that the orbital current contribution is negligible in the Co/Cr sample with $\eta_{L-S}^{Co} \sim 0$. Furthermore, we observe that the ξ_{DLT} of the Gd/Cr sample

decreases with increasing temperature (Supplementary Note 7). This can be attributed to phonon scattering since the orbital angular momentum is strongly coupled to the lattice through the crystal field potential²⁰. At higher temperatures, more phonons are generated, reducing the OHE.

Magnetization switching by efficient $L-S$ conversion through Pt interfacial layer.

We next demonstrate another $L-S$ conversion technique that modifies the NM/FM interface by inserting a Pt layer. This method has the advantage that it can be easily incorporated into perpendicularly magnetized CoFeB/MgO structures, which is a basic component of various spintronic devices^{43–45}. Figure 3a illustrates the conversion process in a Cr/Pt/CoFeB structure, where the L_{OHE} originating from Cr is converted to S_{OHE} in the Pt layer. Since Pt has a positive η_{L-S}^{Pt} due to positive σ_{SH}^{Pt} , S_{OHE} would be positive ($\sigma_{OH}^{Cr}\eta_{L-S}^{Pt} > 0$), while S_{SHE} is negative ($\sigma_{SH}^{Cr} < 0$). Thus, the OHT due to S_{OHE} is the opposite of the spin Hall torque due to S_{SHE} . To examine the effect of Pt insertion on OHT, we perform current-induced magnetization switching experiments as schematically illustrated in Fig. 3b. Figure 3c shows switching curves as a function of pulse current density (J_{pulse}) for Cr (10.0 nm)/Pt (0 or 1.0 nm)/CoFeB (0.9 nm)/MgO (1.6 nm) Hall-bar patterned samples. Note that an in-plane magnetic field B_x of +20 mT is applied along the current direction for deterministic switching of the perpendicular magnetization^{2,4,46}. The Cr/CoFeB sample shows a counter-clockwise switching curve consistent with negative θ_{SH}^{eff} , caused primarily by the SHE in Cr. The switching polarity is reversed by introducing a Pt (1 nm) insertion layer. The clockwise switching curve of the Cr/Pt/CoFeB sample corresponds to positive θ_{SH}^{eff} , which is the expected sign in the OHT scenario (Fig. 3a). The sign reversal of θ_{SH}^{eff} of the samples is also confirmed by perpendicular harmonic Hall measurements (Supplementary Note 8). Note that the switching polarity is abruptly reversed when t_{Pt} is greater than

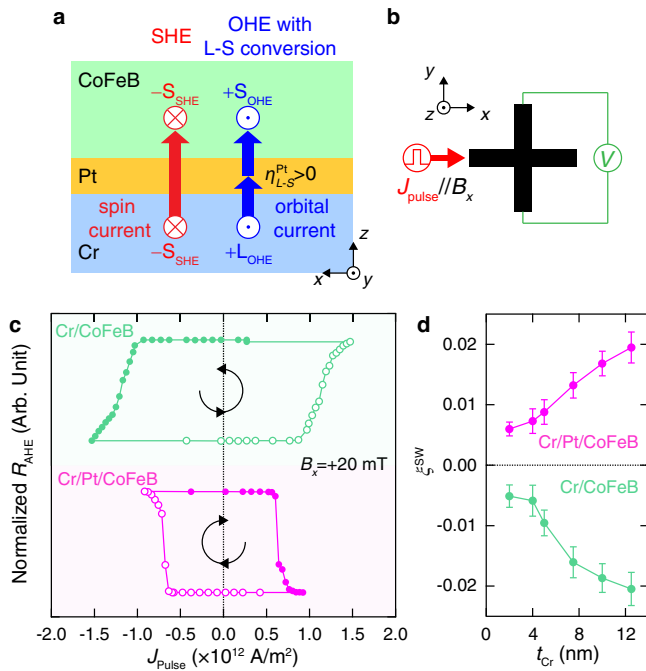


Fig. 3 Orbital-Hall-torque-driven magnetization switching by in Cr/Pt/CoFeB heterostructures. **a** Schematic illustration of the orbital-to-spin conversion by η_{L-S}^{Pt} in the Cr/Pt/CoFeB heterostructure. The spin (orbital) angular momentum is represented by S (L). The source of S and L is marked by the subscript of SHE (OHE) for spin Hall effect (orbital Hall effect). **b** The magnetization switching measurement geometry for a Hall-bar sample, in which an in-plane magnetic field B_x is applied along the pulsed current J_{pulse} . **c** Magnetization switching curves of Cr (10.0 nm)/CoFeB (0.9 nm) and Cr (10.0 nm)/Pt (1.0 nm)/CoFeB (0.9 nm) samples under a B_x of +20 mT. The green and magenta symbols represent the samples without and with the Pt insertion layer, respectively. Open (closed) symbols indicate magnetization switching from down-to-up (up-to-down) directions. The switching polarity is indicated by an arrow in the center of curve. **d** t_{Cr} -dependent switching efficiency (ξ^{SW}) of the Cr/CoFeB (green) and Cr/Pt/CoFeB (magenta) samples. Lines are guide to eyes. All measurements are conducted at 300 K. The error bars in **d** are due to the standard deviation of fittings of $B_C = B_p/\cos\theta$ which is (B_p) estimation. Here, where B_p is the domain wall propagation field, B_C is the coercive field, and θ is the polar angle of the magnetic field (Supplementary Note 10).

0.6 nm (Supplementary Note 9), where Pt forms a continuous film that effectively converts orbital currents to spin currents. This makes the OHE dominant over the SHE.

The sign change in $\theta_{\text{SH}}^{\text{eff}}$ can be caused by the inserted Pt itself with positive $\sigma_{\text{SH}}^{\text{Pt}}$. To rule out this possibility, we investigate the t_{Cr} dependence of the current-induced magnetization switching for the samples, where t_{Cr} ranges from 2.0 to 12.5 nm. Figure 3d shows the switching efficiency^{47,48} $\xi^{\text{SW}} [= (2e/h)(M_S t_{\text{CoFeB}} B_p / J_{\text{SW}})]$ as a function of t_{Cr} . Here, t_{CoFeB} is the CoFeB thickness, B_p is the domain wall propagation field, and J_{SW} is the switching current density (Supplementary Note 10). We find that the magnitude of ξ^{SW} for both samples increases with increasing t_{Cr} , while its sign remains unchanged for all t_{Cr} 's used in this study. Since the contribution of the spin current generated from Pt to $\theta_{\text{SH}}^{\text{eff}}$ in the Cr/Pt/CoFeB structures will decrease with increasing t_{Cr} , the similar thickness dependence of ξ^{SW} indicates that the $\theta_{\text{SH}}^{\text{eff}}$ of both samples predominantly originates from the Cr layer, not from the Pt interfacial layer; the SHE and OHE in Cr are the main sources of $\theta_{\text{SH}}^{\text{eff}}$ for the

Cr/CoFeB and Cr/Pt/CoFeB samples, respectively. These results demonstrate that the OHT can be effectively modified by interface SOC engineering and is capable of switching the perpendicular magnetization.

In conclusion, we experimentally demonstrate non-trivial OHT, spin torques originating from the orbital current in Cr, by introducing two effective ways of orbital-to-spin (L - S) conversion, which is a key ingredient of OHT generation. First, we employ a rare-earth FM of Gd having a larger L - S conversion efficiency than that of conventional 3d FMs. This greatly improves the SOT efficiency of the Cr/Gd bilayers compared to that of the Cr/Co bilayers. Second, we introduce a Pt interfacial layer in the Cr/CoFeB bilayers to facilitate L - S conversion. This allows the OHT to control the perpendicular magnetization in the Cr/Pt/CoFeB heterostructures. Since orbital currents can occur in various materials regardless of the SOC strength, our results provide a unique strategy based on orbital currents to develop material systems with enhanced SOT efficiency.

Methods

Film preparation and Hall-bar fabrication. Bilayers of FM (Co, Ni)/Cr, FM (Co, Ni)/Pt, Gd/Cr, and Co/Cr for harmonic measurements were deposited on Si/SiO₂ or Si/Si₃N₄ substrates using DC magnetron sputtering under a base pressure of $<2.6 \times 10^{-5}$ Pa, while Cr/CoFeB and Cr/Pt/CoFeB structures for switching experiments were deposited on a highly resistive Si substrate using DC and RF magnetron sputtering under a base pressure of $<4.0 \times 10^{-6}$ Pa. An underlayer of Ta (1 nm)/AlO_x (2 nm), or Ta (1.5 nm) layers were used to obtain smooth roughness; a capping layer of Ta (2–3 nm) was used to prevent further oxidation. All metallic layers and the MgO layer were grown with a working pressure of 0.4 Pa and a power of 30 W at room temperature. The AlO_x layer was formed by deposition of an Al layer and subsequent plasma oxidation with an O₂ pressure of 4.0 Pa and a power of 30 W for 75 s. Hall-bar-patterned devices with widths of 5, 10, or 15 μm were defined using photolithography and Ar ion-milling.

Spin-orbit torque characterization. In-plane harmonic measurement with AC current (frequency of 11 Hz) was performed to evaluate the spin-orbit torque of the heterostructures. Both $R_{xy}^{1\omega}$ and $R_{xy}^{2\omega}$ were recorded by two lock-in amplifiers at the same time while varying the azimuthal angle (φ) under a constant external field B_{ext} and a current density J_x of $1 \times 10^{11} \text{ A/m}^2$.

Current-induced magnetization switching measurements. Magnetization switching experiments were conducted by applying a current pulse (pulse width of 30 μs) with a constant external magnetic field (B_x) of +20 mT. The magnetization state was checked by anomalous Hall resistance (R_{AHE}) after applying the current pulse.

Data availability

The data that support the findings of this study are available from the corresponding author upon reasonable request.

Received: 30 March 2021; Accepted: 14 October 2021;

Published online: 01 November 2021

References

1. Sinova, J., Valenzuela, S. O., Wunderlich, J., Back, C. H. & Jungwirth, T. Spin Hall effects. *Rev. Mod. Phys.* **87**, 1213–1260 (2015).
2. Miron, I. M. et al. Perpendicular switching of a single ferromagnetic layer induced by in-plane current injection. *Nature* **476**, 189–193 (2011).
3. Liu, L. et al. Spin-torque switching with the giant spin Hall effect of tantalum. *Science* **336**, 555–558 (2012).
4. Liu, L., Lee, O. J., Gudmundsen, T. J., Ralph, D. C. & Buhrman, R. A. Current-induced switching of perpendicularly magnetized magnetic layers using spin torque from the spin Hall effect. *Phys. Rev. Lett.* **109**, 096602 (2012).
5. Demidov, V. E. et al. Magnetic nano-oscillator driven by pure spin current. *Nat. Mater.* **11**, 1028–1031 (2012).
6. Emori, S., Bauer, U., Ahn, S. M., Martinez, E. & Beach, G. S. D. Current-driven dynamics of chiral ferromagnetic domain walls. *Nat. Mater.* **12**, 611–616 (2013).
7. Ryu, K. S., Thomas, L., Yang, S.-H. & Parkin, S. Chiral spin torque at magnetic domain walls. *Nat. Nanotechnol.* **8**, 527–533 (2013).

8. Manchon, A. et al. Current-induced spin-orbit torques in ferromagnetic and antiferromagnetic systems. *Rev. Mod. Phys.* **91**, 035004 (2019).
9. Ryu, J., Lee, S., Lee, K. J. & Park, B.-G. Current-induced spin-orbit torques for spintronic applications. *Adv. Mater.* **32**, 1907148 (2020).
10. Tanaka, T. et al. Intrinsic spin Hall effect and orbital Hall effect in 4d and 5d transition metals. *Phys. Rev. B* **77**, 165117 (2008).
11. Kontani, H., Tanaka, T., Hirashima, D. S., Yamada, K. & Inoue, J. Giant orbital Hall effect in transition metals: origin of large spin and anomalous Hall effects. *Phys. Rev. Lett.* **102**, 016601 (2009).
12. Go, D., Jo, D., Kim, C. & Lee, H.-W. Intrinsic spin and orbital Hall effects from orbital texture. *Phys. Rev. Lett.* **121**, 086602 (2018).
13. Jo, D., Go, D. & Lee, H.-W. Gigantic intrinsic orbital Hall effects in weakly spin-orbit coupled metals. *Phys. Rev. B* **98**, 214405 (2018).
14. Bhowal, S. & Satpathy, S. Intrinsic orbital moment and prediction of a large orbital Hall effect in two-dimensional transition metal dichalcogenides. *Phys. Rev. B* **101**, 121112(R) (2020).
15. Canonico, L. M., Cysne, T. P., Molina-Sanchez, A., Muniz, R. B. & Rappoport, T. G. Orbital Hall insulating phase in transition metal dichalcogenide monolayers. *Phys. Rev. B* **101**, 161409(R) (2020).
16. Bhowal, S. & Satpathy, S. Intrinsic orbital and spin Hall effects in monolayer transition metal dichalcogenides. *Phys. Rev. B* **102**, 035409 (2020).
17. Bhowal, S. & Vignale, G. Orbital Hall effect as an alternative to valley Hall effect in gapped graphene. *Phys. Rev. B* **103**, 195309 (2021).
18. Cysne, T. P. et al. Disentangling orbital and valley Hall effects in bilayers of transition metal dichalcogenides. *Phys. Rev. Lett.* **126**, 056601 (2021).
19. Go, D. & Lee, H.-W. Orbital torque: torque generation by orbital current injection. *Phys. Rev. Res.* **2**, 013177 (2020).
20. Go, D. et al. Theory of current-induced angular momentum transfer dynamics in spin-orbit coupled systems. *Phys. Rev. Res.* **2**, 033401 (2020).
21. Ding, S. et al. Harnessing orbital-to-spin conversion of interfacial orbital currents for efficient spin-orbit torques. *Phys. Rev. Lett.* **125**, 177201 (2020).
22. Kim, J. et al. Non-trivial charge-to-spin conversion in ferromagnetic metal/Cu/Al₂O₃ by orbital transport. *Phys. Rev. B* **103**, L020407 (2021).
23. Tazaki, Y. et al. Current-induced torque originating from orbital current. Preprint at [arXiv http://arXiv.org/abs/2004.09165](http://arXiv.org/abs/2004.09165) (2020).
24. Ding, S. et al. Observation of the orbital Rashba-Edelstein magnetoresistance. Preprint at [arXiv http://arXiv.org/abs/2105.04495](http://arXiv.org/abs/2105.04495) (2021).
25. Amin, V. P., Li, J., Stiles, M. D. & Haney, P. M. Intrinsic spin currents in ferromagnets. *Phys. Rev. B* **99**, 220405(R) (2019).
26. Wang, W. et al. Anomalous spin-orbit torques in magnetic single-layer films. *Nat. Nanotechnol.* **14**, 819–824 (2019).
27. Avci, C. O. et al. Interplay of spin-orbit torque and thermoelectric effects in ferromagnet/normal-metal bilayers. *Phys. Rev. B* **90**, 224427 (2014).
28. Du, C., Wang, H., Yang, F. & Hammel, P. C. Systematic variation of spin-orbit coupling with *d*-orbital filling: Large inverse spin Hall effect in 3d transition metals. *Phys. Rev. B* **90**, 140407(R) (2014).
29. Chuang, T. C., Pai, C. F. & Huang, S. Y. Cr-induced perpendicular magnetic anisotropy and field-free spin-orbit-torque switching. *Phys. Rev. Appl.* **11**, 061005 (2019).
30. Cui, B. et al. Current induced magnetization switching in Pt/Co/Cr structures with enhanced perpendicular magnetic anisotropy and spin Hall effect. *Appl. Phys. Express* **12**, 043001 (2019).
31. Nguyen, M.-H., Ralph, D. C. & Buhrman, R. A. Spin torque study of the spin Hall conductivity and spin diffusion length in platinum thin films with varying resistivity. *Phys. Rev. Lett.* **116**, 126601 (2016).
32. Zhang, W., Han, W., Jiang, X., Yang, S.-H. & Parkin, S. S. P. Role of transparency of platinum-ferromagnet interfaces in determining the intrinsic magnitude of the spin Hall effect. *Nat. Phys.* **11**, 496–502 (2015).
33. Gambardella, P. & Miron, I. M. Current-induced spin-orbit torques. *Philos. Trans. R. Soc. A* **369**, 3175–3197 (2011).
34. Emori, S. et al. Interfacial spin-orbit torque without bulk spin-orbit coupling. *Phys. Rev. B* **93**, 180402(R) (2016).
35. Amin, V. P. & Stiles, M. D. Spin transport at interfaces with spin-orbit coupling: formalism. *Phys. Rev. B* **94**, 104419 (2016).
36. Amin, V. P. & Stiles, M. D. Spin transport at interfaces with spin-orbit coupling: phenomenology. *Phys. Rev. B* **94**, 104420 (2016).
37. Baek, S.-h. C. et al. Spin currents and spin-orbit torques in ferromagnetic trilayers. *Nat. Mater.* **17**, 509–513 (2018).
38. Lee, H.-Y. et al. Enhanced spin-orbit torque via interface engineering in Pt/CoFeB/MgO heterostructures. *APL Mater.* **7**, 031110 (2019).
39. Krupin, O. et al. Rashba effect at magnetic metal surfaces. *Phys. Rev. B* **71**, 201403(R) (2005).
40. Stöhr, J. & Siegmann, H. C. *Magnetism: From Fundamentals to Nanoscale Dynamics*. Vol. 152 (Springer Series in Solid-state Sciences, 2006).
41. Ueda, K., Pai, C. F., Tan, A. J., Mann, M. & Beach, G. S. D. Effect of rare earth metal on the spin-orbit torque in magnetic heterostructures. *Appl. Phys. Lett.* **108**, 232405 (2016).
42. Zabel, H. Magnetism of chromium at surfaces, at interfaces and in thin films. *J. Phys. Condens. Matter* **11**, 9303–9346 (1999).
43. Ikeda, S. et al. A perpendicular-anisotropy CoFeB-MgO magnetic tunnel junction. *Nat. Mater.* **9**, 721–724 (2010).
44. Torrejon, J. et al. Neuromorphic computing with nanoscale spintronic oscillators. *Nature* **547**, 428–431 (2017).
45. Borders, W. A. et al. Integer factorization using stochastic magnetic tunnel junctions. *Nature* **573**, 390–393 (2019).
46. Qiu, X. et al. Angular and temperature dependence of current induced spin-orbit effective fields in Ta/CoFeB/MgO nanowires. *Sci. Rep.* **4**, 4491 (2014).
47. Lee, O. J. et al. Central role of domain wall depinning for perpendicular magnetization switching driven by spin torque from the spin Hall effect. *Phys. Rev. B* **89**, 024418 (2014).
48. Mishra, R. et al. Anomalous current-induced spin torques in ferrimagnets near compensation. *Phys. Rev. Lett.* **118**, 167201 (2017).

Acknowledgements

We acknowledge fruitful discussion with Hyun-Woo Lee, Kyoung-Wan Kim, and Daegun Jo. We also thank Byoung Kook Kim at the KAIST Analysis Center for Research Advancement (KARA) for his support on the magnetic properties measurement. We acknowledge the Jülich Supercomputing Centre for providing computational resources under project jiff40. This work was supported by the National Research Foundation of Korea (2015M3D1A1070465, 2020R1A2C2010309, and 2020R1A2C3013302) and by the German Research Foundation (Deutsche Forschungsgemeinschaft)—TRR 173—268565370 (project A11), TRR 288—422213477 (project B06).

Author contributions

The study was performed under the supervision of B.-G.P., S.L. and M.-G.K. fabricated samples and conducted the in-plane harmonic measurements and spin-orbit torque switching experiments with the help of D.K., J.-H.K., T.L., G.-H.L., N.J.L., J.K. and S.K. D.G. and Y.M. performed theoretical calculations. S.L., M.-G.K. and B.-G.P. performed data analysis with the help of D.G., K.-J.K. and K.-J.L. S.L., M.-G.K. and B.-G.P. wrote the paper with the help of all authors.

Competing interests

The authors declare no competing interests.

Additional information

Supplementary information The online version contains supplementary material available at <https://doi.org/10.1038/s42005-021-00737-7>.

Correspondence and requests for materials should be addressed to Byong-Guk Park.

Peer review information *Communications Physics* thanks Xiao-long Fan, Sashi Satpathy and the other, anonymous, reviewer(s) for their contribution to the peer review of this work.

Reprints and permission information is available at <http://www.nature.com/reprints>

Publisher's note Springer Nature remains neutral with regard to jurisdictional claims in published maps and institutional affiliations.



Open Access This article is licensed under a Creative Commons Attribution 4.0 International License, which permits use, sharing, adaptation, distribution and reproduction in any medium or format, as long as you give appropriate credit to the original author(s) and the source, provide a link to the Creative Commons license, and indicate if changes were made. The images or other third party material in this article are included in the article's Creative Commons license, unless indicated otherwise in a credit line to the material. If material is not included in the article's Creative Commons license and your intended use is not permitted by statutory regulation or exceeds the permitted use, you will need to obtain permission directly from the copyright holder. To view a copy of this license, visit <http://creativecommons.org/licenses/by/4.0/>.

© The Author(s) 2021